Automotive and Engine Technology (2025) 10:17
https://doi.org/10.1007/s41104-025-00162-w

RESEARCH

# Numerical investigation on spark ignition and flame kernel formation of lean premixed hydrogen/air flame under ICE condition

**Chunkan Yu[1] · Brijesh Kinkhabwala[2] · Chunwei Wu[1] · Sven Eckart[3] · Thomas Koch[2]**

Received: 4 November 2025 / Accepted: 23 November 2025


**Abstract**

The present work investigates the spark ignition and flame kernel formation processes in hydrogen–air mixtures under real engine-relevant conditions from a chemical-physical perspective. A one-dimensional numerical model based on the *INSFLA* solver with cylindrical geometry is used to resolve the coupled effects of detailed chemical kinetics and molecular transport during the ignition phase. The initial and boundary conditions (e.g. initial pressure, initial temperature, equivalence ratio, spark width and duration) are directly taken from a hydrogen-fueled internal combustion engine (H2-ICE) operation point. The simulations capture both failed and successful spark ignition events. Sensitivity analyses identify chain-branching and chain-termination reactions as the dominant chemical kinetic factors controlling the speed of flame kernel formation, while molecular transport effects become significant only after the onset of flame propagation. Furthermore, the evolution of NO emissions is analyzed in detail, showing that thermal NO dominates at high temperatures, whereas the NNH pathway contributes substantially during the early ignition stage, with the $N_2O$ route playing a minor role. Overall, the study provides mechanistic insights into the chemical and transport processes governing early flame development and NO formation in hydrogen-fueled engines, offering a scientific foundation for optimizing spark ignition strategies and reducing NOx emissions under realistic engine conditions.

**Keywords:** Hydrogen combustion · Spark ignition · Flame kernel formation · NOx emission · ICE

## 1 Introduction

The transport sector is increasingly focusing on decarbonisation, as conventional internal combustion engines (ICEs) rely on fossil fuels and emit significant $CO_2$ per unit of energy [1]. Hydrogen, being carbon-free, offers a promising alternative, enabling combustion without $CO_2$ emissions while also reducing CO, unburned hydrocarbons, and soot [2, 3]. When produced from renewable electricity, hydrogen can achieve near-zero $CO_2$-equivalent emissions [3].

In mobility applications, hydrogen is primarily utilized in fuel cells and hydrogen internal combustion engines (H2-ICEs). H2-ICEs are particularly attractive for short- and medium-term decarbonisation because they can leverage existing ICE infrastructure and reduce manufacturing costs compared to fuel-cell systems [2, 4, 5]. As a transitional technology, H2-ICEs combine technological maturity with low-emission operation [6, 7].

Hydrogen shows a relatively high auto-ignition temperature compared to conventional diesel fuel [4]. Consequently, achieving auto-ignition in a hydrogen-fueled compression ignition engine would require an extremely high compression ratio [8]. At the same time, hydrogen requires an extremely low minimum ignition energy and high diffusivity [9–11], thus local hot spots or turbulent regions within the combustion chamber can initiate uncontrolled pre-ignition or knocking well before the charge reaches the theoretical auto-ignition temperature, leading to an unstable combustion engine operation. Therefore, spark-ignition

✉ Chunkan Yu
chunkan.yu@kit.edu

[1] Institute of Technical Thermodynamics, Karlsruhe Institute of Technology, Engelbert-Arnold-Straße 4, 76131 Karlsruhe, Baden-Württemberg, Germany

[2] Institute of Internal Combustion Engines (IFKM), Karlsruhe Institute of Technology, Rintheimer Querallee 2, 76131 Karlsruhe, Baden-Württemberg, Germany

[3] Gas and Heat Technology, Institute of Thermal Engineering, Technical University Bergakademie Freiberg, Gustav-Zeuner-Straße 7, 09599 Freiberg, Sachsen, Germany

Published online: 11 December 2025

(SI) concepts have become the primary focus for hydrogen internal combustion engine (H2-ICE) development [4, 12, 13], as they allow precise control of ignition timing and enable lean-burn operation to enhance thermal efficiency and reduce NOx emissions. Investigating the SI process is critical because it directly affects flame-kernel development, ignition stability, combustion duration and overall engine efficiency, and numerical studies on spark ignition process and flame kernel formation provide valuable insights for optimizing engine design and emission control strategies.

The present work aims to provide a fundamental understanding of the spark ignition process, with particular emphasis on the formation and early development of the flame kernel, as well as the underlying chemical pathways leading to NO formation. From a physico-chemical perspective, this study investigates the complex interactions between chemical kinetics, energy deposition and molecular transport phenomena that govern ignition and early flame propagation in lean hydrogen–air mixtures. To achieve this, a one-dimensional (1D) simulation framework based on the in-house *INSFLA* solver is used under a cylindrical geometry configuration, which captures the essential features of the spark ignition event while allowing detailed resolution of chemical and transport processes, involving a detailed chemical kinetic mechanism for $H_2/O_2$ systems with NOx sub-mechanism.

The present paper is organized as follows. In Sect. 2, the mathematical formulation, including the governing equations, spark ignition model and chemical kinetic mechanism, is briefly outlined with references provided for further details. In Sect. 3, the numerical setup including the boundary and initial conditions derived from real engine tests is introduced. Sect. 4 presents the results and discussion, focusing on flame kernel formation and the accompanying NOx formation from a chemical-kinetic perspective. Finally, Sect. 5 summarizes the key findings and provides an outlook for future research.

## 2 Mathematical modeling

The present work focuses on the early stage of spark ignition and flame-kernel development, during which the flame radius remains small and the kernel remains nearly perfectly symmetric. As shown by recent multidimensional studies such as in [14] where a 3D DNS was performed for a similar spark ignition process in a laminar configuration, the ignition process in this early period is well approximated by a symmetric laminar configuration, and multidimensional effects such as curvature-induced flame acceleration and cellular instability become relevant only after the flame expands beyond a critical radius. The present 1D formulation is therefore intentionally adopted to isolate and analyze the underlying chemical-kinetic and molecular-transport mechanisms governing the initial spark-ignition and flame-kernel establishment.

For the present work, the in-house code *INSFLA* [15] will be used for the computation. In this section, the governing equations used in the numerical simulations are briefly outlined. The detailed chemical kinetic mechanism for the $H_2/O_2$ system, including NOx formation pathways, is also introduced. Furthermore, the simplified spark ignition model applied under idealized conditions is described. Overall, this section provides a concise overview of the computational framework used in the present study.

### 2.1 General governing equations

In general, the governing equations of species mass, momentum, and energy in cylindrical coordinates can be employed to model the spark ignition process using a simplified one-dimensional geometry. The mathematical formulation follows that proposed in [15], in which a Lagrangian coordinate transformation $\psi = \int \rho r^2 \mathrm{d}r$ is introduced to eliminate the convection terms from the governing equations. In this formulation, the continuity equation does not need to be explicitly solved, as it is automatically satisfied under the Lagrangian transformation [15]. Furthermore, as studied in [16], the uniform pressure assumption is valid for a spark duration longer than 0.01 ms, which is also applicable in the present study. Under these assumptions, the governing equations to solve the pressure $p$, temperature $T$ and mass fraction of $i-$th species $w_i$ for $n_s$ species can be simplified to [15, 16]:

$$\frac{\partial r}{\partial \psi} - \frac{1}{\rho r} = 0 \tag{1}$$

$$\frac{\partial p}{\partial \psi} = 0 \tag{2}$$

$$\frac{\partial w_i}{\partial t} + \frac{\partial}{\partial \psi}\left(\rho r w_i V_i\right) - \frac{\dot{\omega}_i M_i}{\rho} = 0 \tag{3}$$

$$\begin{aligned} &\frac{\partial T}{\partial t} - \frac{1}{\rho c_p}\frac{\partial p}{\partial t} - \frac{1}{c_p}\frac{\partial}{\partial \psi}\left(\rho r^2 \lambda \frac{\partial T}{\partial \psi}\right) \\ &\quad + \frac{r^2}{c_p}\sum_{i=1}^{n_s} \rho w_i V_i c_{pi}\frac{\partial T}{\partial \psi} + \frac{1}{\rho c_p}\sum_{i=1}^{n_s}\dot{\omega}_i h_i M_i = \frac{\dot{q}_s}{\rho c_p} \end{aligned} \tag{4}$$

In these equations, we have the variables radius $r$, density $\rho$, isobaric specific heat capacity of the mixture $c_p$, heat conductivity of the mixture $\lambda$, molar mass of species $M_i$, specific enthalpy of species $h_i$, molar formation rate of species

$\dot{\omega}_i$, isobaric heat capacity of species $c_{pi}$. $V_i$ represents the diffusion velocity of species $i$, including the differential diffusion of different species and thermal diffusion (Soret effect) [17].

In Eq. (4), $\dot{q}_s$ is a prescribed spatio-temporal power density, which is also schematic illustrated in Fig. 1, as [16]:

$$\dot{q}_s(r,t) = \begin{cases} \frac{D_s}{\tau_s} \cdot \exp\left[-\left(\frac{r}{r_w}\right)^8\right] & \text{for } 0 \le t \le \tau_s, \\ 0 & \text{otherwise.} \end{cases} \tag{5}$$

Here, $D_s$ is the maximum energy density (J/m$^3$) at $r = 0$, and $r_w$ is the spark width. $\tau_s$ is the spark duration time describing how long the spark energy is provided into the system. For an infinite cylinder which is considered in the present work, the spark ignition energy $E_{SI}$ can be expressed in terms of energy per unit length, with the unit J/m, as follows:

$$\begin{aligned} E_s &= \int_{r=0}^{+\infty} \int_{t=0}^{\tau_s} (2\pi r)\dot{q}_s(r,t)\mathrm{d}t\mathrm{d}r \\ &= \Gamma\left(\frac{5}{4}\right) \cdot \tau_s \cdot \pi r_w^2 \cdot D_s \\ &= 0.9064 \cdot \tau_s \cdot \pi r_w^2 \cdot D_s. \end{aligned} \tag{6}$$

## 2.2 Chemical kinetic model

The chemical kinetic mechanism used in the present study consists of two sub-mechanisms:

(i) The sub-mechanism for the hydrogen/nitrogen/air system is adopted from Maas and Warnatz [15], which consists of 19 reversible elementary reactions including 9 species: $H_2$, $O_2$, $N_2$, H, O, OH, $HO_2$, $H_2O_2$, $H_2O$;

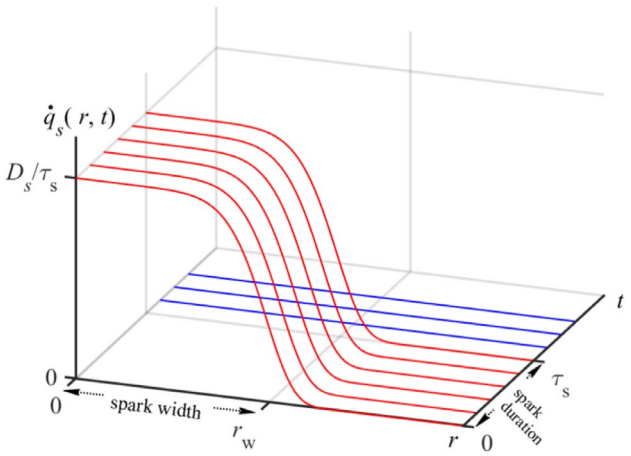


**Fig. 1** Schematic illustration of spark ignition energy over space and time

(ii) The sub-mechanism describing the N–H–O chemistry is taken from Mendiara and Glarborg [18], which consists of 162 reversible elementary reactions including 21 species: NO, $NO_2$, $NO_3$,$N_2O$, HNO, HON, HONO, $HNO_2$, $H_2NO$, HNOH, $HONO_2$, $NH_3$, $NH_2$, NH, N, $N_2$ $H_4$, $N_2$ $H_3$, $N_2$ $H_2$, $H_2NN$, NNH, $NH_2OH$.

The formation of NO in [18] includes key elementary reactions that can be categorized into different mechanistic routes. The first is the thermal NO pathway [19, 20], which primarily involves the elementary reaction between molecular nitrogen and atomic oxygen via $N_2 + O \rightleftharpoons NO + N$. Furthermore, under lean combustion conditions, the flame temperature is generally insufficient to support significant thermal NO formation. In such cases, as studied by reaction pathway analyses in [21], NO production is predominantly controlled by the NNH mechanism, where NNH radicals serve as the main intermediates linking the nitrogen and hydrogen reaction systems. More detailed discussion on the formation of NO under lean conditions can be found in [18, 22].

## 2.3 Comments on current models

It should be noted that the present chemical kinetic mechanism does not include ionization or plasma-related reactions. As will be shown later, the simulated gas-phase temperature after the deposition of spark ignition energy remains below approximately 1300 K, which is far lower than the threshold required for plasma formation [23, 24]. Consequently, plasma-specific processes such as electron impact ionization or recombination are not expected to play a significant role under the present conditions.

Furthermore, it should be emphasized that in this work, a simplified spark energy deposition model is employed, in which the input energy is assumed to be spatially and temporally uniform between the electrodes. This formulation serves as an idealized representation of the energy deposition process, allowing the focus to be placed on the subsequent flame kernel formation and the early stage of flame development under controlled conditions. Similar simplifications have been widely adopted in previous numerical and experimental investigations of spark ignition [25–28], as they have shown reasonable predictive capability for the minimum ignition energy and the onset of flame kernel formation, particularly for idealized laboratory configurations such as explosion-proof vessels [29, 30]. In these experiments, the spark itself corresponds to a realistic discharge similar to those used in internal combustion engines, yet the simplified energy-deposition assumption has proven sufficient for predicting the required ignition energy. Nevertheless, it is acknowledged that this simplification does not fully

capture the physical characteristics of a real spark discharge, which typically undergoes distinct breakdown, arc and glow phases. These phases differ substantially in discharge voltage, current, plasma temperature and consequently in the local thermo-chemical evolution. More detailed modeling of these processes, including plasma dynamics and ionization kinetics, is the subject of our ongoing research [31–33].

## 3 Numerical setup under engine-relevant condition

To ensure that the present one-dimensional (1-D) simulations using *INSFLA* are representative of realistic engine-relevant conditions, this section describes the setup and boundary parameters used for the calculations. The selected parameters, including the initial pressure $p_0$ and temperature $T_0$, relative air-fuel ratio $\lambda$, as well as the spark duration $\tau_s$ and spark width $r_{\mathrm{w}}$, are not arbitrarily chosen. Instead, they are determined based on typical values observed in hydrogen-fueled internal combustion engines (H2-ICEs). By performing the numerical configuration with experimentally relevant conditions, the present model aims to capture the essential physics of the spark ignition and flame kernel formation processes while maintaining computational simplicity.

The subject engine is a single-cylinder heavy-duty engine developed for demanding transportation applications. . The baseline engine originally operated on diesel fuel. For the present study, the engine was converted to hydrogen port fuel injection operation through modifications to the piston geometry, resulting in a compression ratio of 10.5:1.

All experimental investigations were performed in a state-of-the-art engine test cell facility equipped with a steady-state dynamometer. A range of sensors and actuators were employed to monitor and control engine operation. A Kistler pressure transducer was utilized for high-frequency in-cylinder pressure measurement, while an FLD 4000 analyzer was used for NOx quantification. Additional advanced instrumentation and a comprehensive data acquisition system were implemented to ensure precise measurement of engine performance and emission parameters. For the numerical investigation, the engine test case setup was defined based on the specifications summarized in Table 1.

**Table 1** Engine test case setup

| Parameter | Value |
|---|---|
| Bore | 140 mm |
| Stroke | 170 mm |
| Compression ratio | 10.5:1 |
| Engine speed | 1100 rpm |
| Relative air–fuel ratio | 2.5 |

The hydrogen port fuel injection (PFI) engine was experimentally characterized in the test cell, and in parallel, a computational fluid dynamics (CFD) model was developed using CONVERGE CFD software. The CFD model was subsequently validated against the experimental in-cylinder pressure and emission data, confirming its reliability for further analysis. The present article outlines the methodology adopted for the analysis of flame kernel propagation, which utilizes experimentally derived boundary conditions and thermodynamic properties as inputs to the CFD model. For detailed investigation, the mid-load operating point corresponding to approximately 15 bar indicated mean effective pressure (IMEP) was considered. A standard J-gap iridium spark plug with a spark gap $r_{\mathrm{w}}$ of 0.2 mm was employed. The spark duration was fixed at $\tau_s$ =1.5 ms, and the relative air–fuel ratio $\lambda$ was maintained at 2.5. At the onset of ignition, the in-cylinder pressure and temperature were approximately $p_0$ =20 bar and $T_0$ =600 K, respectively. These experimentally derived boundary conditions were subsequently adopted for the one-dimensional (1D) simulation in *INSFLA* studies to ensure consistency between the numerical and experimental analyses.

## 4 Results and discussion

As discussed in the last section, we will use for the following calculation the setup from a real engine condition, namely the initial temperature $T_0 = 600$ K, initial pressure $p_0 = 2$ MPa. The gas mixture is the complete premixed hydrogen/air mixture with relative air-fuel ratio $\lambda = 2.5$. For the spark ignition process, the spark width is chosen as 0.2 mm, and the spark duration time is 1.5 ms. Furthermore, if not specified, all numerical calculations are based on detailed transport model involving the differential diffusion of different species and thermal diffusion (Soret effect).

### 4.1 Failed and successful spark ignition processes

To discuss the phenomenon of flame kernel formation, this section begins with a comparative examination of the failed and successful spark ignition processes. The ignition process can be observed from the temporal and spatial evolution of the temperature field, which serves as a key diagnostic indicator of the underlying energy deposition. It should be explicitly mentioned again here that the temperature reported below represents the gas-phase thermodynamic temperature. The maximum temperature during and after the deposition of spark ignition energy is well below typical plasma temperatures, and thus plasma-specific temperatures such as rotational or electron temperature are not applicable.

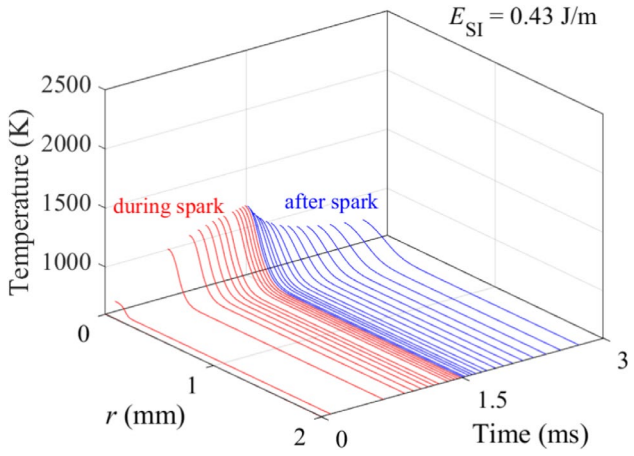


**Fig. 2** Temporal development of the spatial temperature during the spark (red curve) and after the spark (blue curve)

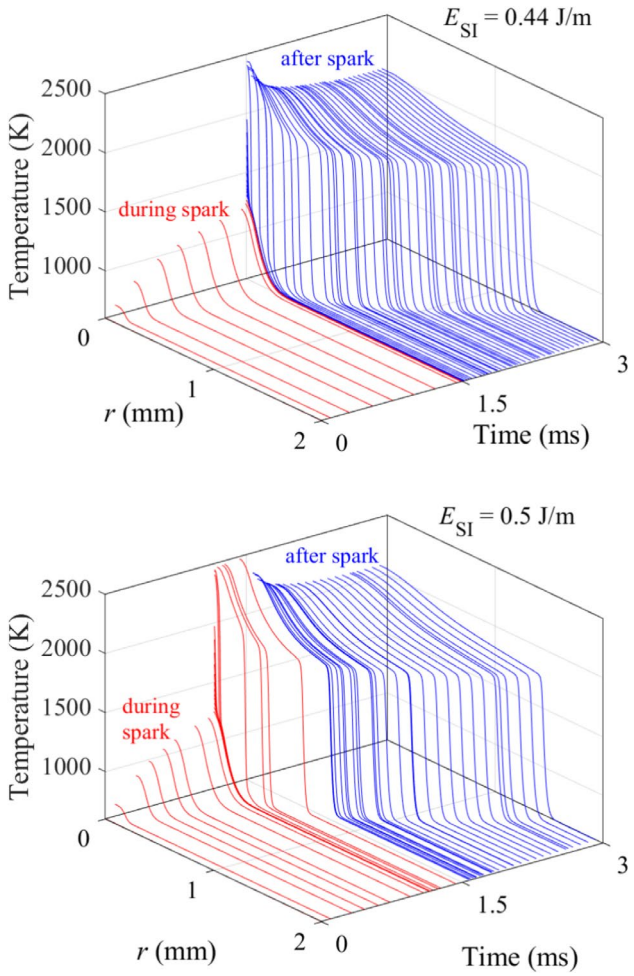


**Fig. 3** Temporal development of the spatial temperature during the spark (red curve) and after the spark (blue curve) for two different spark ignition energy $E_{SI}$

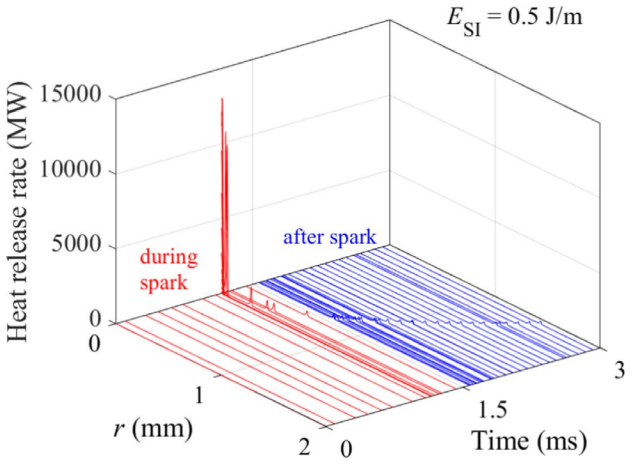


**Fig. 4** Temporal development of the spatial heat release rate (HRR) during the spark (red curve) and after the spark (blue curve) for spark ignition energy $E_{SI} = 0.5$ J/m

Figure 2 presents the temporal evolution of the spatial temperature distribution during and after the spark at an energy level of $E_{SI} = 0.43$ J/m, corresponding to a failed spark ignition case. During the spark phase (red curves), localized heating at and near the center occurs due to the spark energy deposition, resulting in a transient rise in the central temperature. However, after the termination of the spark (blue curves), the temperature remains below the critical level required to support chain-branching reactions and radical pool buildup. Consequently, no flame kernel is formed, and the accumulated thermal energy dissipates through heat conduction, leading to a slow temperature decay towards a quasi-homogeneous temperature field.

In contrast to the failed ignition case, Fig. 3 illustrates two examples of successful spark ignition events obtained at $E_{SI} = 0.44$ J/m and $E_{SI} = 0.5$ J/m, respectively. In both cases, the temperature profiles clearly show a rapid rise at the center ($r = 0$), which marks the onset of flame kernel formation. Once the kernel is initially formed, a self-sustaining flame front develops and propagates outward. Although both cases result in successful ignition, the timing of the kernel formation differs. At $E_{SI} = 0.44$ J/m, the flame kernel forms shortly after the deposition of spark ignition energy. In contrast, at $E_{SI} = 0.5$ J/m, the kernel formation occurs already during the spark phase, suggesting that the spark ignition energy is high enough to enable an immediate initiation of exothermic reactions within the heated region.

## 4.2 Flame kernel formation

In this section, the process of flame kernel formation during spark ignition is discussed in detail. The heat release rate (HRR) serves as an effective indicator for characterizing the intensity of chemical energy release, which can be

calculated as $\mathrm{HRR} = -\sum_{i=1}^{n_s} \dot{\omega}_i h_i$. Figure 4 presents the temporal evolution of the spatial HRR distribution during the spark phase (red curves) and after the spark phase (blue curves) for the case of $E_{\mathrm{SI}} = 0.5$ J/m. To further illustrate the temporal behavior, Fig. 5 shows the HRR at the center $r = 0$ (green curve) and the maximum HRR within the domain (purple curve) as functions of time. For optical clarity, the plotted time window in this figure corresponds to the period of flame kernel formation and the early stage of flame propagation. At the initial stage, the HRR remains low because chemical reactions proceed slowly. As self-ignition occurs near the center, a rapid temperature rise is accompanied by a sharp increase in HRR as well, indicating the occurrence of strong chemical reaction. During this period, the HRR at the center coincides with the maximum HRR, suggesting that the strongest reaction occurs within the central region. As the flame kernel forms and subsequent flame propagation begins, the peak HRR is observed in the flame front zone, while the HRR at the center decreases noticeably as the local chemical reactions approach completion.

Since the peak value of HRR corresponds to the region of the strongest chemical reactions, it typically locates at the flame front zone. Therefore, the position of the maximum HRR can be defined as the flame front position $r_f$ [34–36], and its temporal evolution is shown on the right y-axis in Fig. 5. The slope of flame front position ($\mathrm{d}r_f/\mathrm{d}t$) can be interpreted as the quasi-propagation speed of the flame front. It can be observed that during the flame kernel formation stage, the flame front rapidly expands outward, as indicated by the steep slope of $r_f$. Subsequently, as the flame develops and propagates further into the surrounding unburnt gas mixture, the propagation speed decreases and eventually approaches an almost constant value.

To further characterize the time required for forming a self-sustaining flame, the time corresponding to the maximum slope of $r_f$ (the point where $\mathrm{d}r_f/\mathrm{d}t$ reaches its peak) is defined as the flame kernel formation delay time (FkfDT). This quantity represents the time needed to form a flame kernel capable of supporting stable flame propagation. The definition of FkfDT is conceptually analogous to the ignition delay time (IDT), as both are governed by the accumulation of reactive radicals via chain propagation and chain branching steps.

#### 4.2.1 Effect of chemical reactions

To investigate which key elementary reactions control the early stage of flame kernel formation, Fig. 6 presents the relative sensitivity of FkfDT with respect to various elementary reactions. A negative sensitivity indicates that accelerating the corresponding reaction rate leads to a shorter FkfDT, thereby promoting earlier flame kernel formation. From this

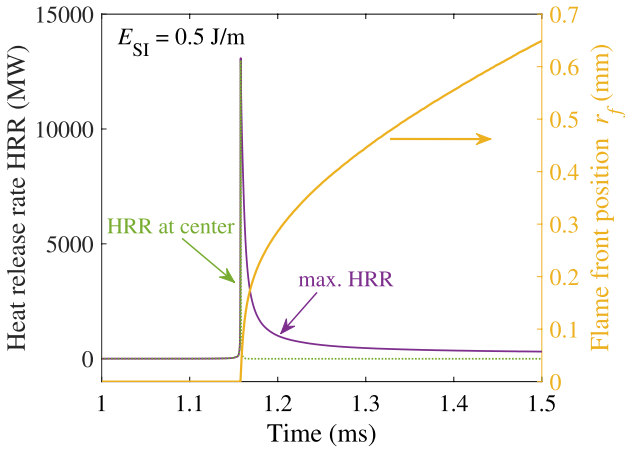


**Fig. 5** Left y-axis: HRR at the center $r = 0$ (green curve) and the maximum HRR within the domain (purple curve) as functions of time; Right y-axis: Flame front position $r_f$ over time. The case corresponds to Fig. 4

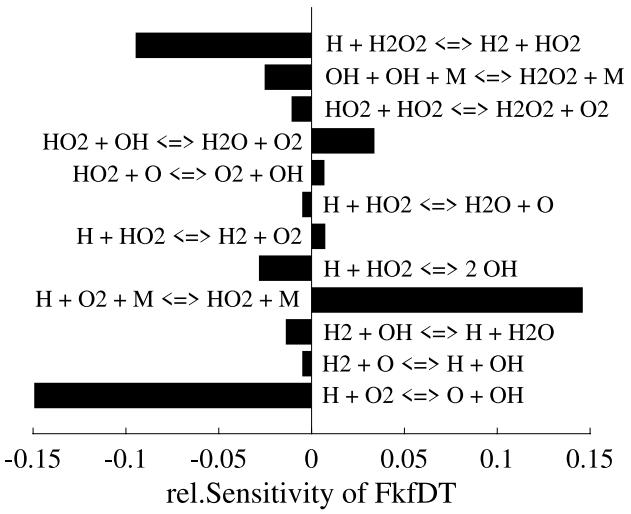


**Fig. 6** Relative sensitivity of flame kernel formation delay time (FkfDT) with respect to various elementary reactions

figure, it is observed that the sensitivity represents a strong similarity to that of the IDT, with the most influential reactions corresponding to chain-branching step (i.e. $\mathrm{H{+}O_2} \rightleftharpoons \mathrm{OH{+}O}$) and chain-termination step (i.e. $\mathrm{H{+}O_2{+}M} \rightleftharpoons \mathrm{HO_2{+}M}$). The increased importance of chain-termination reactions can be attributed to the high-pressure conditions under which spark ignition occurs, where accompanied higher third-body concentrations significantly enhance termination pathways.

#### 4.2.2 Effect of molecular transport

After discussing the influence of chemical reactions on flame kernel formation, the role of molecular transport in

this process will be investigated. To understand this effect, two additional molecular transport models were considered:

- a model accounting for differential diffusion among species while neglecting thermal diffusion, and
- a simplified model employing the unity Lewis number assumption, in which all species share the same diffusion velocity.

Figure 7 presents the temporal evolution of the flame front position for the case of $E_{\mathrm{SI}} = 0.5$ J/m under all three molecular transport models. It is evident that during the early stage of flame development (before the flame kernel formation delay time (FkfDT)) the choice of transport model shows no influence on the formation of the flame front. This can be straightforwardly explained by the fact that, in this stage, flame kernel formation is primarily driven by the accumulation of radicals leading to self-ignition, a process that is chemistry-controlled rather than transport-controlled. Once the flame front is established and begins to propagate outward, molecular transport effects become increasingly significant, influencing the subsequent flame propagation behavior.

#### 4.2.3 Effect of spark ignition energy $E_{\mathrm{SI}}$

The spark ignition energy $E_{\mathrm{SI}}$ also shows a significant influence on the flame kernel formation process. To illustrate this effect, Fig. 8 presents the time development of the flame front position $r_f$ under three different $E_{\mathrm{SI}}$ conditions. It can be clearly observed that increasing $E_{\mathrm{SI}}$ enhances the temperature within the spark-heated region, thereby promoting chemical reactions. As a result, a higher $E_{\mathrm{SI}}$ leads to a faster flame kernel formation. This trend is further quantified in Fig. 9, where the flame kernel formation delay time (FkfDT) is shown to decrease monotonically with increasing $E_{\mathrm{SI}}$ within the successful spark ignition regime. The reduction in FkfDT with higher $E_{\mathrm{SI}}$ confirms that stronger energy deposition accelerates radical accumulation and shortens the time required to generate a self-sustaining flame kernel.

Once the flame kernel is established and outward propagation begins, it can be observed that the evolution of the flame front position with time becomes nearly identical for different $E_{\mathrm{SI}}$ cases. To further quantify the propagation of the burned mixture into the unburned region, the stretched propagation speed with respect to the burned mixture, $S_{\mathrm{L,b}} = \mathrm{d}r_f/\mathrm{d}t$, is defined following the approach proposed in [37]. Figure10 presents the variation of $S_{\mathrm{L,b}}$ as a function of the flame front position $r_f$ for three different $E_{\mathrm{SI}}$ values (the corresponding temporal evolution of the flame front position can be found in Fig. 8).

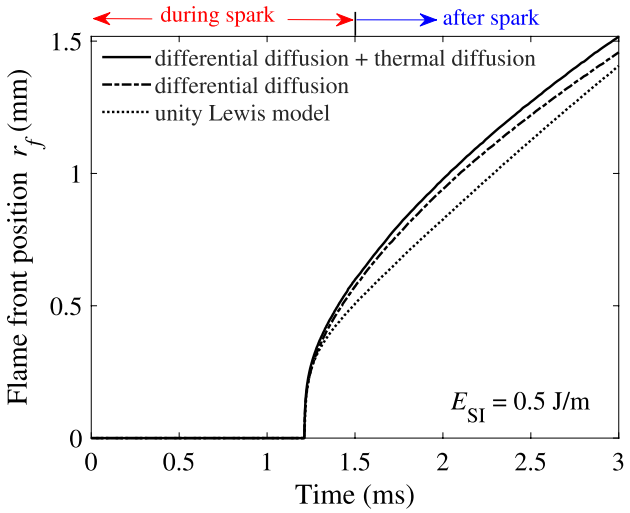


**Fig. 7** Flame front position $r_f$ over time using three different molecular transport models using $E_{\mathrm{SI}} = 0.5$ J/m. The case using differential diffusion + thermal diffusion corresponds to Fig. 4

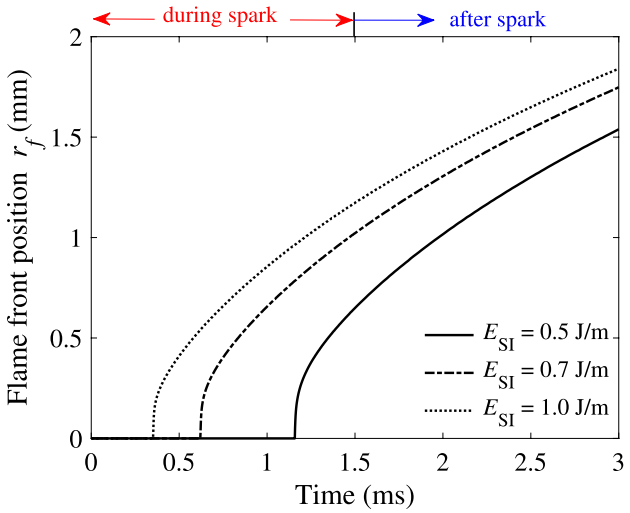


**Fig. 8** Flame front position $r_f$ over time using three different spark ignition energy $E_{\mathrm{SI}}$

It can be clearly observed that, regardless of the spark ignition energy applied, once the flame kernel is formed and starts to propagate outward, the stretched propagation speed $S_{\mathrm{L,b}}$ shows nearly identical behavior at the same flame front position. This indicates that, after flame kernel formation, the subsequent flame propagation is primarily governed by chemical-thermal coupling and transport processes, rather than by the initial spark energy input.

### 4.3 Formation of nitric oxides

For hydrogen-fueled ICE, nitric oxides (NOx) emissions represent a critical environmental concern. Therefore, this subsection focuses on the formation characteristics of NO,

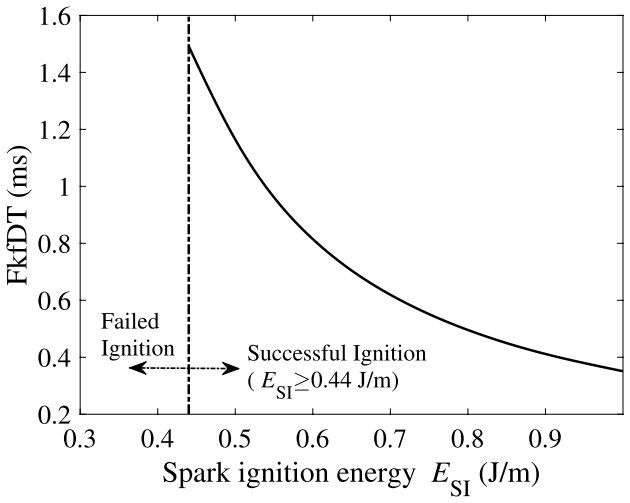


**Fig. 9** The dependence of flame kernel formation delay time (FkfDT) on spark ignition energy $E_{\mathrm{SI}}$

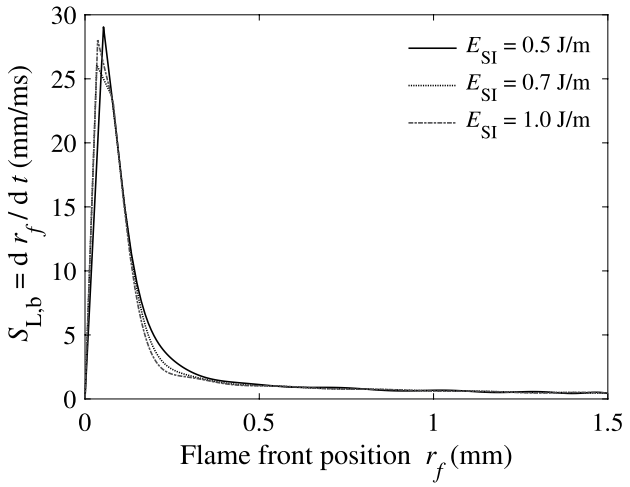


**Fig. 10** Stretched propagation speed with respect to the burned mixture $S_{\mathrm{L,b}}$=d$r_f$/d$t$ over flame front position $r_f$ using three different spark ignition energy $E_{\mathrm{SI}}$. The time evolution of flame front position $r_f$ can be found in Fig. 8

$NO_2$ and $N_2O$ during the entire spark ignition and flame kernel formation processes.

Figure 11 presents the temporal evolution of these three species for the case of $E_{\mathrm{SI}} = 0.5$ J/m, while the corresponding temperature development is shown in Fig. 3 (below). It can be clearly observed that NOx formation occurs rapidly immediately after successful ignition, corresponding to the phase with sharp temperature rise. Among the three species, NO is the dominant emission, with its concentration approximately two orders of magnitude higher than those of $N_2O$ and $NO_2$. It should be noted that, although under high-pressure conditions NO can also be generated via the nitrous oxide $N_2O$ mechanism in the presence of a third-body molecule following $N_2 + O(+M) \rightleftharpoons N_2O(+M)$ [19, 20, 38], the predominance of NO over $NO_2$ and $N_2O$

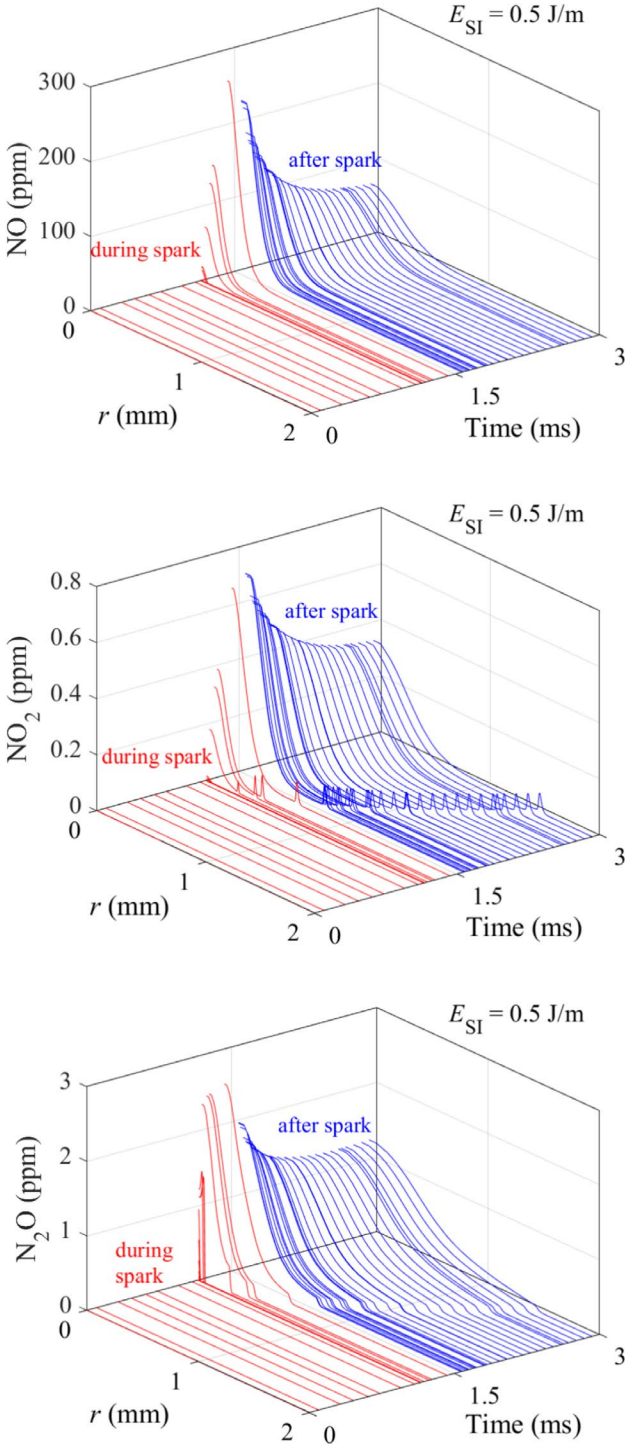


**Fig. 11** Temporal development of the spatial NO, $NO_2$ and $N_2O$ concentration in ppm during the spark (red curve) and after the spark (blue curve) for $E_{\mathrm{SI}} = 0.5$ J/m

remains consistent across different $E_{\mathrm{SI}}$ levels. Therefore, in the following, we will focus on investigating the formation of NO.

Since the NO concentration reaches its maximum at the center region $r = 0$ during the ignition and flame kernel

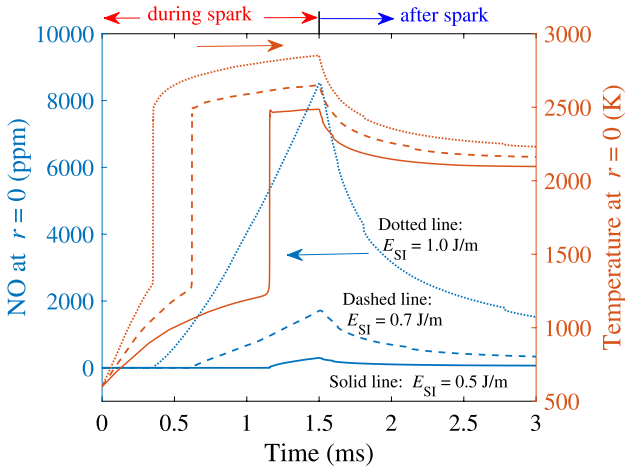


**Fig. 12** NO concentration (left blue y-axis) and temperature (right red y-axis) at the center $r = 0$ over time using three different spark ignition energy $E_{SI}$

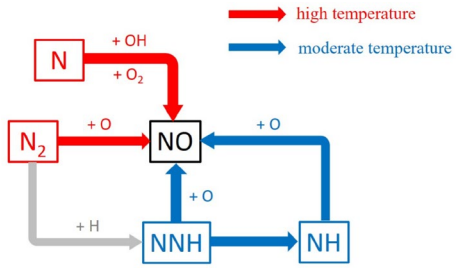


**Fig. 13** Reaction path for the formation of NO at high temperature (red) and moderate temperature (blue)

formation stages, Fig. 12 illustrates the temporal evolution of NO at this location for three different spark ignition energies $E_{SI}$, shown on the left blue y-axis. Given the strong temperature dependence of NO formation [20, 39], the corresponding temperature at the center $r = 0$ is plotted on the right red y-axis as well. This dual-axis representation enables a direct comparison between the thermal evolution and NO generation behavior under varying spark ignition energies. It can be clearly observed that, unlike the sharp temperature rise during ignition, the increase in NO concentration occurs more gradually. As the spark ignition energy $E_{SI}$ increases, the corresponding center temperature rises, leading to a significant enhancement in NO formation. In the present cases shown in Fig. 12, when $E_{SI}$ increases from 0.5 to 1.0 J/m, the peak central temperature rises from approximately 2500 K to 3000 K, while the maximum NO concentration increases by nearly three orders of magnitude.

To further understand the formation pathways of NO, a reaction path analysis was performed at the location where the NO concentration reaches its maximum. The analysis shows that the NO peak coincides spatially with the region of maximum temperature, indicating that thermal NO formation (Zel'dovich mechanism) [19, 20] is the dominant pathway under the present conditions:

$$N_2 + O \rightleftharpoons NO + N, \quad N + O_2 \rightleftharpoons NO + O, \quad \text{and} \quad N + OH \rightleftharpoons NO + H.$$

These reaction steps are also schematic illustrated in Fig. 13 in red flow.

However, when the reaction path analysis is applied at the location corresponding to the maximum temperature rise rate ($\max(\mathrm{d}T/\mathrm{d}t)$), the way to generate NO changes noticeably. At this stage, the local temperature is still around 1600 K, which is insufficient for efficient thermal NO formation. Consequently, the thermal NO route becomes less dominant, and the NNH pathway becomes the most important mechanism for NO formation (c.f. Fig. 13, blue flow) via

$$NNH + O \rightleftharpoons NO + NH, \quad \text{and} \quad NH + O \rightleftharpoons NO + H,$$

with the initiation step $N_2 + H \rightleftharpoons NNH$. This analysis is consistent with the one also observed in lean premixed hydrogen/air flame in e.g. [21, 40].

## 5 Conclusion

In this work, a one-dimensional cylindrical model based on the *INSFLA* solver was used to investigate the spark ignition and flame kernel formation processes in lean hydrogen/air mixtures under engine-relevant conditions, with boundary and initial parameters (initial pressure, initial temperature, equivalence ratio, spark width and spark duration) derived directly from a hydrogen-fueled internal combustion engine. The numerical model includes detailed chemical kinetics and molecular transport formulation (differential diffusion of different species and thermal diffusion), allowing for a fundamental understanding of the coupled thermal, chemical and transport phenomena during spark ignition and flame kernel formation. The results from the numerical simulation can be summarized as:

- successful ignition occurs only when the central temperature exceeds the threshold required for radical pool buildup and chain-branching reactions. In failed cases, insufficient energy deposition leads to the dissipation of heat through heat conduction outward without flame kernel formation. In general, flame kernel formation can be considered as the temporal development of the heat release rate (HRR) and the spatial evolution of the flame front position. The flame kernel formation delay time (FkfDT) was defined as a quantitative measure of the time required for establishing a self-sustaining flame.

Sensitivity analysis showed that FkfDT is governed by chain-branching ($H+O_2 \rightleftharpoons OH+O$) and chain-termination ($H+O_2+M \rightleftharpoons HO_2+M$) reactions, analogous to the sensitivity analysis observed in ignition delay phenomena.

- The influence of molecular transport was further evaluated by comparing different diffusion models. It was found that during the early ignition stage, molecular transport effects are negligible, confirming that flame kernel formation is chemistry-controlled. However, once the flame kernel is established, differential diffusion become important in determining flame propagation characteristics.
- Varying the spark ignition energy $E_{SI}$ indicated that higher energy deposition accelerates radical accumulation, thereby reducing FkfDT. Despite this, the subsequent flame propagation after kernel formation was nearly identical across different $E_{SI}$ levels, indicating that the flame behavior after kernel formation is primarily controlled by chemical and molecular transport processes rather than by the initial spark energy input.
- The formation of nitric oxides (NOx) during spark ignition and flame kernel development was analyzed. The results showed that NO is the dominant nitrogen oxide species, with concentrations approximately two orders of magnitude higher than $NO_2$ and $N_2O$. The reaction path analysis identified thermal NO (Zeldovich mechanism) as the main formation route at high temperatures, while the NNH route becomes key mechanism in the early ignition stage via $NNH+O \rightleftharpoons NO+NH$ and $NH+O \rightleftharpoons NO+H$. These findings provide a consistent kinetic interpretation of NO formation across varying spark energies and temperature regimes.

We acknowledge that the 1D model does not capture the multidimensional phenomena that dominate real engine environments. Instead, the present study provides high-resolution, chemistry-detailed a priori insights such as reaction sensitivities, competing NO-formation pathways, and the dependence of kernel-formation delay on transport models and spark energy, which can guide future multidimensional simulations and turbulent-ignition modeling.

Overall, the present study offers fundamental insights into the chemical kinetics, molecular transport and NOx emission behavior governing spark ignition and early flame development in hydrogen-fueled internal combustion engines. Ongoing work aims to extend the current modeling framework by developing a more comprehensive spark discharge model capable of resolving the distinct breakdown, arc, and glow phases, as well as plasma-assisted chemistry to capture ionization and non-equilibrium effects. These future improvements will enhance the predictive accuracy of spark ignition modeling under realistic engine conditions and support the optimization of hydrogen combustion systems for clean and efficient operation.

**Acknowledgements** We are indebted to the CONVERGE CFD team for granting an educational license that made this work possible. Support from the state of Baden-Württemberg through bwHPC is likewise gratefully recognized.

**Author Contributions** Conceptualization: C.Yu; Methodology: C.Yu, C.Wu, S.Eckart; Software and simulations: C.Yu, C.Wu, E.Kinkhabwala; Validation: C.Yu; Data analysis: C.Yu, E.Kinkhabwala; Writing-original draft preparation: C.Yu, E.Kinkhabwala; Writing - review and editing: E.Kinkhabwala, C.Wu, S.Eckart, T.Koch; All authors have reviewed the manuscript.

**Funding** Open Access funding enabled and organized by Projekt DEAL.

**Data Availability** No datasets were generated or analysed during the current study.

## Declarations

**Conflict of interest** The authors declare that they have no Conflict of interest.



## References

1. Demirbas, A.: Correlations between carbon dioxide emissions and carbon contents of fuels. Energy Sources B **1**(4), 421–427 (2006)
2. Onorati, A., Payri, R., Vaglieco, B.M., Agarwal, A.K., Bae, C., Bruneaux, G., Canakci, M., Gavaises, M., Günthner, M., Hasse, C., et al.: The Role of Hydrogen for Future Internal Combustion Engines. Sage Publications, London (2022)
3. Salvi, B.L., Subramanian, K.: Sustainable development of road transportation sector using hydrogen energy system. Renew. Sustain. Energy Rev. **51**, 1132–1155 (2015)
4. Verhelst, S., Wallner, T.: Hydrogen-fueled internal combustion engines. Prog. Energy Combust. Sci. **35**(6), 490–527 (2009)
5. Kim, J., Moon, I.: The role of hydrogen in the road transportation sector for a sustainable energy system: a case study of Korea. Int. J. Hydrogen Energy **33**(24), 7326–7337 (2008)
6. Kapus, P., Raser, B., Arnberger, A., Heindl, R., Egert, M., Kunder, N., Fraidl, G., Weissbäck, M., Grabner, P.: High efficiency hydrogen internal combustion engine—carbon free powertrain for

passenger car hybrids and commercial vehicles. In: Proceedings of the International Vienna Motor Symposium 2022, pp. 1–20. Österreichischer Verein für Kraftfahrzeugtechnik (2022)
7. Halder, P., Babaie, M., Salek, F., Haque, N., Savage, R., Stevanovic, S., Bodisco, T.A., Zare, A.: Advancements in hydrogen production, storage, distribution and refuelling for a sustainable transport sector: hydrogen fuel cell vehicles. Int. J. Hydrogen Energy **52**, 973–1004 (2024)
8. Szwaja, S., Grab-Rogalinski, K.: Hydrogen combustion in a compression ignition diesel engine. Int. J. Hydrogen Energy **34**(10), 4413–4421 (2009)
9. Crowl, D.A., Jo, Y.-D.: The hazards and risks of hydrogen. J. Loss Prev. Process Ind. **20**(2), 158–164 (2007)
10. Bane, S., Ziegler, J., Boettcher, P., Coronel, S., Shepherd, J.: Experimental investigation of spark ignition energy in kerosene, hexane, and hydrogen. J. Loss Prev. Process Ind. **26**(2), 290–294 (2013)
11. Ono, R., Nifuku, M., Fujiwara, S., Horiguchi, S., Oda, T.: Minimum ignition energy of hydrogen-air mixture: effects of humidity and spark duration. J. Electrostat. **65**(2), 87–93 (2007)
12. Ciniviz, M., Köse, H.: Hydrogen use in internal combustion engine: a review. Int. J. Autom. Eng. Technol. **1**(1), 1–15 (2012)
13. Karagöz, Y., Balcı, Ö., Köten, H.: Investigation of hydrogen usage on combustion characteristics and emissions of a spark ignition engine. Int. J. Hydrogen Energy **44**(27), 14243–14256 (2019)
14. Chu, H., Berger, L., Grenga, T., Wu, Z., Pitsch, H.: Effects of differential diffusion on hydrogen flame kernel development under engine conditions. Proc. Combust. Inst. **39**(2), 2129–2138 (2023)
15. Maas, U., Warnatz, J.: Ignition processes in hydrogen–oxygen mixtures. Combust. Flame **74**(1), 53–69 (1988)
16. Maas, U., Raffel, B., Wolfrum, J., Warnatz, J.: Observation and simulation of laser induced ignition processes in O2–O3 and H2–O2 mixtures. In: Symposium (International) on Combustion, vol. 21, pp. 1869–1876. Elsevier (1988)
17. Hirschfelder, J.O., Curtiss, C.F., Bird, R.B.: The Molecular Theory of Gases and Liquids. Wiley (1964)
18. Mendiara, T., Glarborg, P.: Ammonia chemistry in oxy–fuel combustion of methane. Combust. Flame **156**(10), 1937–1949 (2009)
19. Konnov, A., Colson, G., De Ruyck, J.: No formation rates for hydrogen combustion in stirred reactors. Fuel **80**(1), 49–65 (2001)
20. Warnatz, J., Maas, U., Dibble, R.W.: Combustion: Physical and Chemical Fundamentals, Modeling and Simulation, Experiments, Pollutant Formation. Springer (2006)
21. Day, M.S., Bell, J.B., Gao, X., Glarborg, P.: Numerical simulation of nitrogen oxide formation in lean premixed turbulent H2/O2/N2 flames. Proc. Combust. Inst. **33**(1), 1591–1599 (2011)
22. Skottene, M., Rian, K.E.: A study of NOx formation in hydrogen flames. Int. J. Hydrogen Energy **32**(15), 3572–3585 (2007)
23. Ju, Y., Sun, W.: Plasma assisted combustion: dynamics and chemistry. Prog. Energy Combust. Sci. **48**, 21–83 (2015)
24. Starikovskiy, A., Aleksandrov, N.: Plasma-assisted ignition and combustion. Prog. Energy Combust. Sci. **39**(1), 61–110 (2013)
25. Wu, C., Chen, Y.-R., Schießl, R., Shy, S.S., Yu, C., Maas, U., et al.: Experimental and numerical investigation of the induced ignition process in ammonia/air and ammonia/hydrogen/air mixtures. Proc. Combust. Inst. **40**(1–4), 105466 (2024)
26. Wang, L., Mao, X., Li, J., Wei, H., Shu, G., Pan, J.: Role of hydrogen enrichment in ammonia forced ignition at elevated pressures. Combust. Flame **272**, 113908 (2025)
27. Fernández-Tarrazo, E., Gómez-Miguel, R., Sánchez-Sanz, M.: Minimum ignition energy of hydrogen-ammonia blends in air. Fuel **337**, 127128 (2023)
28. Lu, H., Liu, F., Wang, K., Xu, G., Curran, H.J.: Numerical study on the minimum ignition energy of a methane–air mixture. Fuel **285**, 119230 (2021)
29. Roth, D., Sharma, P., Haeber, T., Schiessl, R., Bockhorn, H., Maas, U.: Ignition by mechanical sparks: ignition of hydrogen/air mixtures by submillimeter-sized hot particles. Combust. Sci. Technol. **186**(10–11), 1606–1617 (2014)
30. Essmann, S., Markus, D., Maas, U.: Investigation of the spark channel of electrical discharges near the minimum ignition energy. Plasma Phys. Technol. **3**(3), 116–121 (2016)
31. Grüninger, M., Toedter, O., Koch, T.: Optical analysis of ignition sparks and inflammation using background-oriented Schlieren technique. Energies **17**(6), 1274 (2024)
32. Michler, T., Toedter, O., Koch, T.: Spatial and time resolved determination of the vibrational temperature in ignition sparks by variation of the dwell time. SN Appl. Sci. **2**(7), 1311 (2020)
33. Michler, T., Toedter, O., Koch, T.: Measurement of temporal and spatial resolved rotational temperature in ignition sparks at atmospheric pressure. Autom. Eng. Technol. **5**(1), 57–70 (2020)
34. Chen, X., Wang, Y., Zirwes, T., Zhang, F., Bockhorn, H., Chen, Z.: Heat release rate markers for highly stretched premixed CH4/air and CH4/H2/air flames. Energy Fuels **35**(16), 13349–13359 (2021)
35. Xing, J., Pillai, A.L., Kurose, R.: Heat release rate surrogate for ammonia-hydrogen premixed flames under various conditions. Appl. Energy Combust. Sci. **15**, 100193 (2023)
36. Zirwes, T., Zhang, F., Habisreuther, P., Hansinger, M., Bockhorn, H., Pfitzner, M., Trimis, D.: Identification of flame regimes in partially premixed combustion from a quasi-DNS dataset. Flow Turbul. Combust. **106**(2), 373–404 (2021)
37. Hesse, R., Bariki, C., Hegetschweiler, M.J., Linteris, G.T., Pitsch, H., Beeckmann, J.: Elucidating the challenges in extracting ultra-slow flame speeds in a closed vessel—a CH2F2 microgravity case study using optical and pressure-rise data. Proc. Combust. Inst. **39**(2), 1783–1792 (2023)
38. Glarborg, P., Miller, J.A., Kee, R.J.: Kinetic modeling and sensitivity analysis of nitrogen oxide formation in well-stirred reactors. Combust. Flame **65**(2), 177–202 (1986)
39. Turns, S.R., et al.: Introduction to Combustion, vol. 287. McGraw-Hill, New York (1996)
40. Capurso, T., Laera, D., Riber, E., Cuenot, B.: Nox pathways in lean partially premixed swirling H2-air turbulent flame. Combust. Flame **248**, 112581 (2023)